RSC Advances

PAPER

View Article Online
View Journal | View Issue

Cite this: *RSC Adv.*, 2017, **7**, 40286

Prepared MnO_2 with different crystal forms as electrode materials for supercapacitors: experimental research from hydrothermal crystallization process to electrochemical performances

Xiaoyu Zhao, *[a] Yongdan Hou,[b] Yanfei Wang,*[a] Libin Yang,[a] Liang Zhu,[a] Ruge Cao[c] and Zuoliang Sha[a]

The aim of this study was to prepare manganese dioxide with different crystal forms through hydrothermal treatment of $MnSO_4 \cdot H_2O$–$KMnO_4$ precursors at various precursor ratios, temperatures, time periods, and pH values. The effect of the preparation parameters on the crystal structure and electrochemical performance of MnO_2 was also studied. The conditions for the preparation of each crystal of MnO_2 were experimentally optimized. The results indicate that the varied parameters affect the crystal form of MnO_2; the ratio of the precursor and reaction temperature are the significant factors affecting the crystal form of MnO_2, and the reaction time and pH value mainly affect the integrity of crystallization. Moreover, the presence of the cations K^+ and NH_4^+ assists the crystallization of α-MnO_2. δ-MnO_2 and amorphous MnO_2 have higher specific capacitance. The specific capacitance is determined not only by the crystal form, but also by the parameters of hydrothermal treatment.

Received 7th June 2017
Accepted 28th July 2017

DOI: 10.1039/c7ra06369e

rsc.li/rsc-advances

1 Introduction

Supercapacitors can be categorized into electric double-layer capacitors and faradaic pseudocapacitors based on the mechanism of charge storage.[1] The former store energy by forming electric double layers between the electrode and the electrolyte, whereas the latter make use of highly reversible chemical intercalation and deintercalation of electrolytic ions at the surface, or in-phase of electroactive species or redox reactions of electrolytic ions at the electrode to store electric charges.[2] The charging and discharging behaviours of faradaic pseudocapacitors are quite similar to those of electric double-layer capacitors; however, in the case of electric double-layer capacitors, the electrode potential is proportional to the loaded electric charges, the voltage is linear to the applied time, and the detected current is almost constant.[3] It has been proven[4] that faradaic process can not only prolong the working time, but also increase the specific capacitance of the capacitor. Due to both the interactions of the electrolytic ions with the surface and in-phase of electroactive species, the energy density stored in this process will be 10–100 times higher than that stored *via* only a superficial process.[5]

As electrode materials of supercapacitors, metallic oxides are believed to have higher faradaic pseudocapacitance rather than the electric double-layer capacitance formed at the surface of the carbon electrode. The faradaic pseudocapacitance can be induced not only at the interface of the electrode|electrolyte, but also inside metallic oxides *via* fast and reversible redox reactions; therefore, the energy is stored in a three-dimensional space, which improves the utilization rate of materials to provide a relatively high specific capacitance and energy density.[6]

Manganese dioxide (MnO_2) as an electrode material for supercapacitors is of great potential. In faradaic pseudocapacitors, the merits of the MnO_2 electrode material are as follows: high theoretical specific capacitance, wide potential window, rich reserves, environmental friendliness, *etc.* However, the low conductivity (10^{-5} to 10^{-6} S cm^{-1}) and unstable structure of MnO_2, leading to poor electrochemical cyclability, limit its application. To overcome these problems, many researchers have tried to design a nano-MnO_2 structure to improve the electrochemical behaviour. It has been reported that the electrochemical performance of MnO_2 depends on the surface area, morphology, and crystal structure and its features.[7,8]

The mechanism of energy storage by MnO_2 materials is generally of two types. First is *via* surface adsorption–desorption: H^+ or basic ions C^+ (Li^+, Na^+, and K^+) adsorb at the surface

[a]*Tianjin Key Laboratory of Marine Resources and Chemistry, College of Chemical Engineering and Materials Science, Tianjin University of Science and Technology, Tianjin 300457, China. E-mail: xyz@tust.edu.cn; wangyanfei@tust.edu.cn*

[b]*Collage of Engineering, Kwame Nkrumah University of Science and Technology, Ghana*

[c]*College of Food Engineering and Biotechnology, Tianjin University of Science and Technology, Tianjin 300457, China*

of electrode to store charges. Second is *via* electron–proton transfer: charges is stored *via* fast and reversible redox reactions, *via* which H^+ or basic ions C^+ (Li^+, Na^+, and K^+) intercalate in or deintercalate out of both the surface materials and materials inside the crystal structure. Reaction equations are given as follows (eqn (1-1) and (1-2)):

$$(MnO_2)_{surface} + M^+ + e^- \leftrightarrow (MnO_2 \cdot M)_{surface} \quad (1\text{-}1)$$

$$MnO_2 + M^+ + e^- \leftrightarrow MnOOM \quad (1\text{-}2)$$

where M^+ stands for Li^+, Na^+, or K^+. During tunnel deintercalation, it has been proven by Toupin *et al.*[9] *via* XPS analysis that there is valent variation of Mn^{4+}/Mn^{3+}. Kuo *etc. et al.*[10] using the *in situ* XRD method found periodical changes in the crystal lattice of MnO_2 during the deintercalation process. Both the abovementioned reports laid the foundation for the second energy storage mechanism of MnO_2. Furthermore, Song *et al.*[11] proposed the energy storage mechanism *via* lattice defects. Normally, the energy storage mechanism of amorphous materials is superficial adsorption and desorption and that of crystal materials is electron–proton transfer.[12,13] Therefore, the electrochemical performance of MnO_2 materials depends on the crystal structure, surface morphology, and grain size, among which, the effect of crystal structure on the electrochemical performance of manganese dioxide and its composites cannot be neglected.[12,14]

Zhang *et al.*[15] prepared MnO_2 with different kinds of crystal structures and morphologies *via* redox reactions of potassium permanganate and sodium nitrite using a hydrothermal process. They also found that nano-α-MnO_2 ball with a low crystalline degree demonstrated a very high specific capacitance of 200 F g^{-1}. Rusi *et al.*[16] also prepared α-MnO_2 with a low crystalline degree, but through electrochemical deposition in a manganese acetate tetrahydrate electrolyte. The prepared α-MnO_2 characterized by cyclic voltammetry test in the Na_2SO_4 electrolyte at a scan rate of 1 mV s^{-1} showed a high specific capacitance of 238 F g^{-1} and good stability; after cycling for 1900 times, the capacitance retention was 84%. Myeongjin Kim *et al.*[17] also prepared graphene oxide (GO)/MnO_2 *via* one-step hydrothermal crystallization as compared to reduced graphene oxide (rGO) prepared by reducing GO with hydrazine hydrate and phosphate acid; needle-shaped MnO_2 grew on reduced graphene oxide to form H-rGO/MnO_2 and S-rGO/MnO_2. In cyclic voltammetry test, the needle-shaped MnO_2 loaded onto reduced graphene oxide forming nano-composites of H-rGO/MnO_2 shows a high specific capacitance of 327.5 F g^{-1} in a 1 M $NaSO_4$ electrolyte at a scan rate of 10 mV s^{-1}. Previous researchers have achieved ideal results with beautiful nano-architectures and excellent electrochemical performance with the aim of enhancing the capacity *via* few specific technologies, for example, heterogeneous doping,[18–24] morphological design and control,[25–30] crystal structure design and selection,[31–33] and so on, which are indeed effective in enhancing the capacity and conductance of MnO_2. However, no systematic research on the hydrothermal crystallization process of powder MnO_2 considering all operating parameters and electrochemical performances for different crystal forms of MnO_2 has been reported to date. Herein, $MnSO_4 \cdot H_2O$–$KMnO_4$ was applied as a precursor. By varying the ratio of the precursor, reaction temperature, time, and pH value, α-MnO_2, β-MnO_2, and δ-MnO_2 were prepared. The effect of cationic dopant on the crystal form of MnO_2 was also examined. Finally, the electrochemical properties of prepared MnO_2 with different crystal forms were studied for its applications in supercapacitors.

2 Experiments

2.1 Preparation of MnO_2

All the chemicals used were of analytical grade. Non-purified polycrystalline MnO_2 was simply prepared *via* one-step hydrothermal synthesis. The classical synthesis procedures are as follows: different designed amounts of potassium permanganate ($KMnO_4$) were weighed and dissolved in 60 mL distilled water. When it was fully dissolved, the pH value of the solution was adjusted by adding 1 M H_2SO_4 or $NH_3 \cdot H_2O$. After the addition of $MnSO_4 \cdot H_2O$ to the above mentioned solution, a black precipitate was formed. The solution was then stirred at room temperature for 30 min and then transferred into a 100 mL Teflon reactor, which was later placed in an incubator for hydrothermal reaction. The reactor was removed after different reaction times and then naturally cooled down to room temperature. The filtered residue was washed with distilled water till the filtrate became neutral. Finally, the solid product was frozen and dried. By changing the ratio of $MnSO_4 \cdot H_2O : KMnO_4$, time duration of the hydrothermal process, pH value, and amount of additive cations, powder MnO_2 with different crystal forms was obtained.

2.2 X-ray diffraction characterization of MnO_2

X-ray diffraction was used to characterize the phase and weight percentage of manganese dioxides prepared under the conditions of different $MnSO_4 \cdot H_2O : KMnO_4$ ratios, hydrothermal treatment time durations, pH values, and cations doped.

2.3 Assembly of electrodes

(I) Porous nickel foam was used as a current collector and cut into 2.5 × 2 cm^2 as a matrix of electrode sheet, which was later washed with acetone for 10 min, distilled water for 5 min, 1 M HCl for 20 min, distilled water for 5 min, and anhydrous ethanol for 5 min. After washing, the cut foam was dried in an incubator at 50 °C for eight hours and then pressed and weighed. The weight was obtained as *m*.

(II) Powered active species, acetylene black, and polyvinylidene fluoride (PVDF) were mixed in the ratio of 8 : 1 : 1. An appropriate amount of *N*-methyl pyrrolidone (NMP), as a binder, was added to sufficiently wet the powder. Through magnetic stirring and ultrasonication, the powder mixture and the binder were uniformly mixed.

(III) The abovementioned mixture was blade coated on nickel foam and then placed in a drying oven at 50 °C to remove the solvent. The active species-loaded nickel foam was then pressed into an electrode sheet, the weight of which was

obtained as m_1; the mass of the active species was calculated from the difference in mass before and after they were coated on nickel foam.

(IV) The electrode sheet was placed in the prepared 1 M Na_2SO_4 electrolyte till it was completely wet; after this, the electrochemical test was carried out.

2.4 Electrochemical test

Ivium potentiostat was used for cyclic voltammetry (CV), galvanostatic charge–discharge (GCD), electrochemical impedance spectroscopy (EIS) analyses of electrode materials. A three-electrode system was applied, in which the active species, platinum wire (Pt), and saturated calomel electrode (SCE) were used as the working electrode, counter electrode, and reference electrode, respectively. The electrolyte applied was 1 M $NaSO_4$. The potential window for the CV test was 0–0.8 V, and the frequency range for the EIS test was from 100 kHz to 0.01 Hz.

3 Results and discussion

3.1 Factors of hydrothermal process influencing the MnO_2 crystal forms

Fig. 1 shows the XRD patterns of both α-MnO_2 and β-MnO_2.[15] On comparing the graphs of two different crystals, it was observed that the diffraction angles of characteristic peaks of both α-MnO_2 and β-MnO_2 were 12.744° and 56.586°, respectively, *via* ratio of which, for instance, $I_{12.744°}/(I_{12.744°} + I_{56.586°})$, the relative amount of α-MnO_2 was obtained.

Fig. 2(a) displays the XRD patterns of MnO_2 obtained *via* hydrothermal synthesis at different ratios of the $MnSO_4 \cdot H_2O$–$KMnO_4$ precursor. It can be observed from Fig. 2(a) that when the ratio was 3 : 2, the product was β-MnO_2; when the ratio was 1 : 1, α-MnO_2 appeared; when the ratio was 3 : 4.5, the amount of α-phase increased; with a decrease in the amount of $MnSO_4 \cdot H_2O$, the ratio became 3 : 9, and the peaks of the products δ-MnO_2 and trace amount of Mn_3O_4 were observed at the diffraction angles of 36.091°, 36.487°, 38.033°, and 44.425°. The presence of Mn_3O_4 with poor crystallinity might be caused by the little amount formed immediately when $MnSO_4 \cdot H_2O$ and $KMnO_4$ reacted with each other, or by crystal defects.

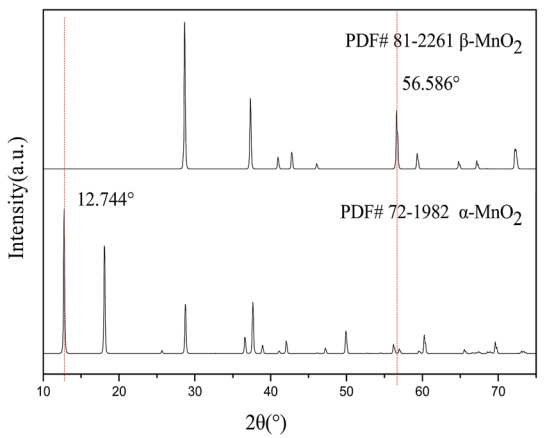

Fig. 1 XRD patterns of α-MnO_2 and β-MnO_2.

The analysis indicates that when the ratio of $MnSO_4 \cdot H_2O$: $KMnO_4$ is reduced, MnO_2 with a β-phase and mixtures of β- and α-phase and α-phase and δ-phase is obtained. There are three reasons for the formation of these products: first, K^+ intercalates into the crystal lattice of MnO_2 to support the lattice and form a larger [2 × 2] tunnel structure. Second, K^+ preferentially adsorbs at the surface of [MnO_6]; this decreases the surface energy of [MnO_6], leading the co-edge of [MnO_6] unit to form a [2 × 2] tunnel structure. Third, from the viewpoint of crystallization, with a constant quantity of $KMnO_4$ but reduced quantity of $MnSO_4 \cdot H_2O$, the degree of supersaturation of the crystallized product decreased, which influenced the nucleation of the crystal to form MnO_2 with different phases. The slower the reaction, the lower the supersaturation level; under this condition, α-MnO_2 is more likely to be formed. With the increasing amount of $KMnO_4$, when $MnSO_4 \cdot H_2O$: $KMnO_4$ reaches 3 : 9, δ-MnO_2 is obtained *via* the hydrothermal treatment at 180 °C for 5 h. The formed δ-MnO_2 with a larger surface area and stratified structure was shaped *via* the rearrangement of [MnO_6] units induced by an increase in the concentration of potassium ions.

Based on the abovementioned discussion, the summary can be drawn as follows: in the $MnSO_4 \cdot H_2O$–$KMnO_4$ system, if $MnSO_4 \cdot H_2O$: $KMnO_4$ ≥3 : 2, the product of hydrothermal crystallization is β-MnO_2. If the ratio of $MnSO_4 \cdot H_2O$ to $KMnO_4$ falls between 3 : 4.5 and 1 : 1, the product is a mixture of β- and α-MnO_2. If $MnSO_4 \cdot H_2O$: $KMnO_4$ falls between 3 : 12 and 3 : 9, the product is δ-MnO_2. Furthermore, [MnO_6] unit in β-MnO_2 forms single-stranded octahedron *via* the common edge and extends along the crystal axis to form a [1 × 1] tunnel structure. However, the channel is very small (0.189 nm in diameter) with few crystal defects and water to support the movement of cations. However, the [MnO_6] unit in α-MnO_2 forms single- or double-stranded octahedron *via* the common edge and [1 × 1] and [2 × 2] tunnel structures, between which the [1 × 1] channel is hollow, but small (0.189 nm in diameter), and the [2 × 2] channel with a diameter of 0.46 nm is helpful for basic ions (such as K^+) to intercalate and deintercalate. Interestingly, δ-MnO_2, with a special stratified structure with an interspacing of 0.7 nm, is beneficial for the free transportation of charged ions, protons, electrons, *etc.*, which further enhances the transfer coefficient of electrons for ion exchange or redox reactions, leading to no damage of the crystal stratified structure.

Fig. 2(b) displays the XRD results of the effect of time duration of hydrothermal treatment on the crystal forms of MnO_2. It can be observed from Fig. 2(b) that the relative amounts of β-MnO_2 are 72.9%, 68.4%, and 64.6% for 5 h, 10 h, and 15 h treatment, respectively. The amount of β-MnO_2 decreases with the increasing treatment time; this indicates that the mixture formed in the first three hours has poor thermal stability and, therefore, continuously transforms into β-MnO_2 under treatment. Therefore, hydrothermal treatment of 3 h will be preferred for forming α-MnO_2 with good crystallinity. During the hydrothermal treatment, the reaction time was proven to have a significant influence on the growth of nano-materials;

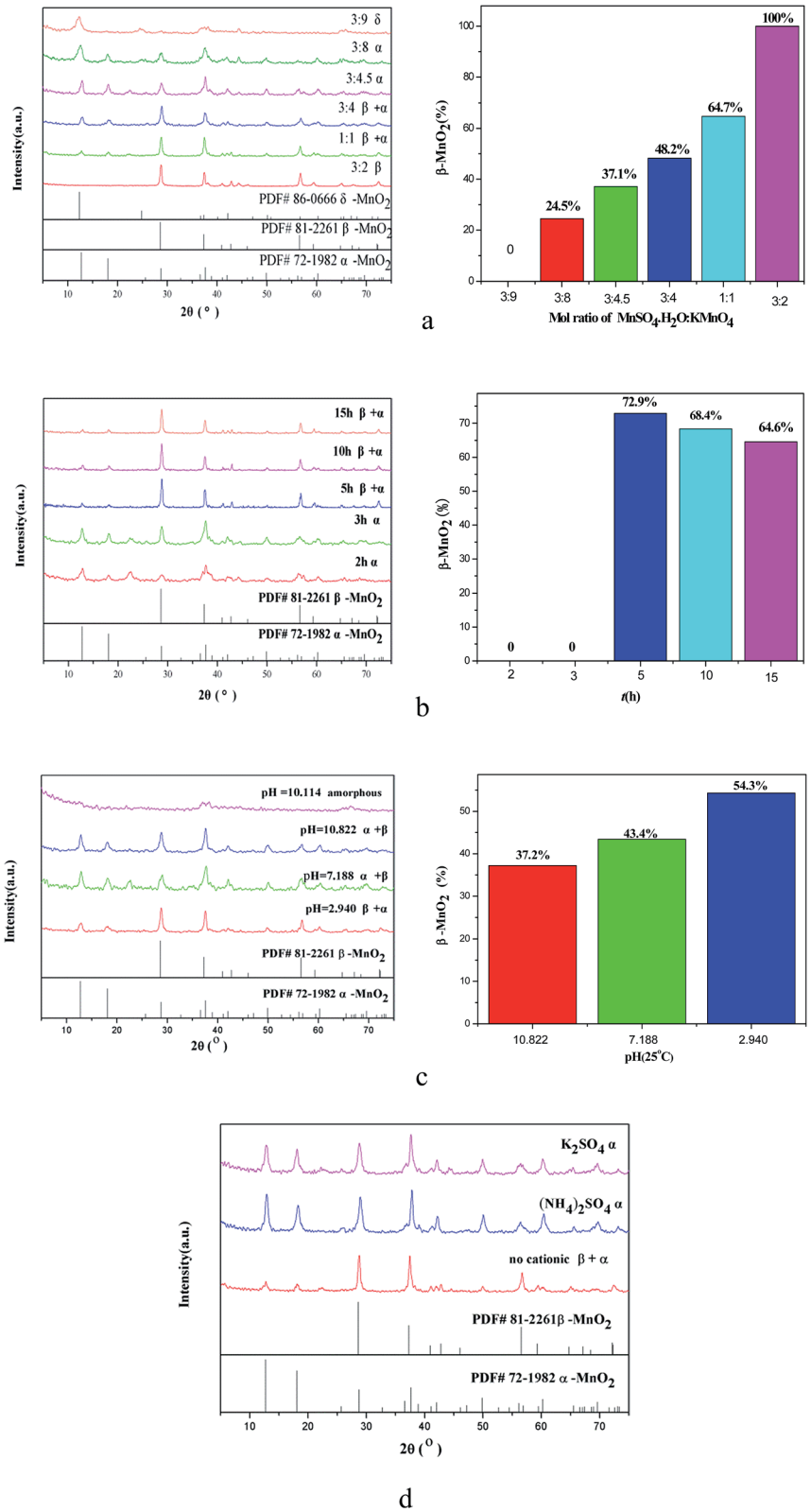

Fig. 2 XRD patterns of MnO_2 obtained by hydrothermal synthesis (a) at different ratios, (b) different reaction times, (c) different pH values, and (d) different cations doped.

moreover, Yang *et al.*[14] have reported that the growth of crystal and its morphology were controlled by a curing process. As the curing time increases, large grains continue to grow completely, but small grains gradually disappear to feed the growth of large grains due to different solubilities of large and small grains, which was driven by reduction of surface energy. Within 3–5 h,

the transformation from α- to β-phase can occur due to a relatively higher K^+ concentration induced by re-crystallization.

Fig. 2(c) shows the XRD results of crystal forms of MnO_2 prepared at different pH values. It can be observed from Fig. 2(c) that the product is a mixture of 66.7% β-MnO_2 and α-MnO_2 with good crystallinity at a pH value of 2.940 adjusted by 1 mol L^{-1} H_2SO_4; however, the product at neutral is 43.4% β-MnO_2 with poor crystallinity, whereas the β-MnO_2 content in the product becomes 37.2% with good crystallinity at a pH value of 10.822 adjusted by 1 mol L^{-1} $NH_3 \cdot H_2O$. The percentage of product under different pH conditions indicates that when the concentration of cations is higher than the concentration of H^+ ions, the product is mainly α-MnO_2 with a [2 × 2] tunnel structure. It has been reported that by adjusting the pH value, the optimum matched degree of hydrolysis can be controlled;[34] this further clarifies that the pH value mainly affects the solubility of the precursor, causing the presence of [MnO_6] unit in different aggregates with various solubilities and degrees of hydrolysis. Therefore, this is consistent with the experimental result that acidic environment is helpful for the growth of β-MnO_2, but basic environment is beneficial for the formation of α-MnO_2. With the $MnSO_4 \cdot H_2O : KMnO_4$ ratio of 1 : 1, a temperature of 150 °C, reaction time of 5 h, and a pH value ranging from 2 to 10, the mixtures of β- and α-MnO_2 were obtained as the products of the hydrothermal process.

Fig. 2(d) illustrates the XRD results of the crystal forms of MnO_2 prepared with different amounts of cations doped. The products obtained under the conditions of a precursor ratio of 1 : 1, 180 °C, and 5 h were mixtures of β- and α-MnO_2. However, the crystal form started to transform when the cations were doped into the system. In detail, [MnO_6] octahedron with a common edge forms β-MnO_2 with a [1 × 1] single-stranded channel along the *C* axis, which later transforms to a double-stranded channel. The double-stranded octahedron shares a common apical angle with the single-stranded octahedron to form α-MnO_2 with a [1 × 1] + [2 × 2] tunnel structure. Besides this, K^+, H^+, NH_4^+, and H_2O can support the large crystal lattice without damage, enlarge the path of cations and electrons, and enhance the transport coefficient. The main contribution to the improvement is likely to be the different surface energy of [MnO_6] octahedrons, which caused the variation of the linking forms among the octahedrons units leading to the appearance of crystal defects, finally, causing the formation of channels and vugular channels with different unit cell parameters.

3.2 Electrochemical characterizations

Using cyclic voltammetry curves to calculate the specific capacitance, the value of charges is obtained by integrating the CV curve. Based on the weight of the active species on the electrode, the specific capacitance can be calculated using the eqn (2-1):

$$C = \frac{\int I \mathrm{d}V}{m v V} \tag{2-1}$$

where *V* is the electrode potential (V), *I* is the responding current (A), *v* is the scanning rate (mV s^{-1}), and *m* is the mass of the electroactive materials (g).

The calculation of the specific capacitance *via* GCD curves is shown in eqn (2-2):

$$C = \frac{I\Delta t}{m\Delta E} \tag{2-2}$$

where *I* is the charging–discharging current, *m* is the mass of the electroactive materials, Δt is the time for discharging, and ΔE is the voltage variation during charging or discharging. The electrochemical properties of various crystal forms of MnO_2 are shown in Fig. 3.

Fig. 3(a) shows the cyclic voltammetry curves of α-MnO_2 prepared under various conditions at a scan rate of 10 mV s^{-1}. It can be observed that all eight α-MnO_2 samples display quasi-rectangular CV curves without obvious redox peaks between 0 and 0.5 V and 0 and 0.8 V against the SCE reference electrode; this indicates relatively good capacitive characteristics.[35] In particular, the α-MnO_2 sample prepared at 100 °C held for 5 h exhibits the highest absolute responding current within the commonly wide potential window from 0 to 0.8 V against the SCE reference electrode; this suggests the better capacitance characteristics under the control of potential limit of hydrogen and oxygen evolution in an aqueous electrolyte.

Fig. 3(b) and (c) show the cyclic voltammetry curves of α- and β-MnO_2 and δ-MnO_2, respectively, prepared under various conditions at a scan rate of 10 mV s^{-1}. The existence of both electric double-layer capacitance and faradaic pseudocapacitance can be realized through quasi-rectangular CV curves and minor redox reaction peaks in all the samples in both Fig. 3(b) and (c).

The quasi-rectangular CV curves indicate the presence of adsorption and desorption processes at the interface of electrode|electrolyte (electric double layers). In Fig. 3(b), in particular, the CV curve of the α + β-MnO_2 sample, prepared at a 1 : 1 ratio of precursor and a pH value of 2.940 and hydrothermally treated at 150 °C for 5 h, shows the largest closed area among all the α + β-MnO_2 samples, suggesting better electrochemical property in the potential window of 0–0.8 V.

Symmetrical redox peaks in both Fig. 3(b) and (c) indicate good reversible faradaic processes.[36] In Fig. 3(c), the minor redox peaks for δ-MnO_2 are induced by storage of charges through free tunnel deintercalation of electrolytic ions (hydrated Na^+, 0.358 nm in radius) within a two-dimensional stratified structure with a 0.7 nm spacing of layers. Generally, the more sufficient the redox reactions occurring through electrons and electrolytic ions with electrode crystals, the higher the reaction peaks; the faster the reactions, the sharper the peaks in the CV curves. Therefore, the CV curves of δ-MnO_2 show a quick response (sharp peak) to current steering, as shown in Fig. 3(c), indicating a fast reaction resulting from small inner resistance; however, the CV curves of β-MnO_2 show irregular shapes with a small closed area, but better rectangular shape, which indicates good capacitive properties.

To obtain more information on how suitable the products are for electrode materials of supercapacitors, galvanostatic charge–discharge tests were performed on different crystal forms of MnO_2 in 1 M Na_2SO_4 at 0.5 A g^{-1}, as illustrated in Fig. 3(d). The plots obtained are nearly linear, indicating that

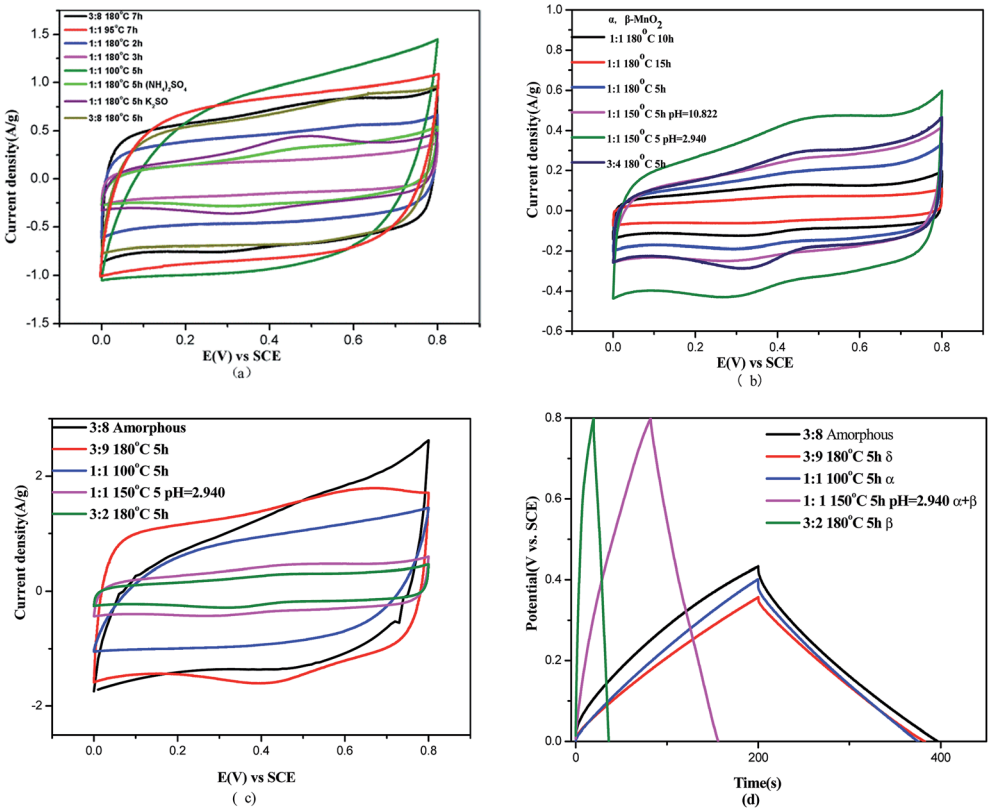

Fig. 3 (a) CV curves of α-MnO_2 under different reaction conditions; (b) CV curves of α- and β-MnO_2 under different reaction condition; (c) CV curves of polymorphous MnO_2 at 10 mV s^{-1}; and (d) GCD curves of polymorphous MnO_2 at a current density of 0.5 A g^{-1}.

the prepared MnO_2 have good pseudocapacitive characterization. The specific capacitances were 286, 111.6, 26.8, and 3.1 F g^{-1} for δ-, α-, α + β-, and β-MnO_2, respectively. Obviously, δ-MnO_2 exhibits best specific capacitance. α-MnO_2 has a 1D structure with (2 × 2) and (1 × 1) tunnels,[37] whereas δ-MnO_2 has a 2D layered structure.[38] Protons can be intercalated into the wide (2 × 2) tunnels (~4.6 Å) of α-MnO_2 and in between the layers (~7 Å) of 2D δ-MnO_2. The presence of narrow (1 × 1) tunnels in β-MnO_2 makes it unsuitable for capacitor application because it cannot accommodate cations during charge–discharge cycling.[37]

The cyclic voltammetry curves of δ-MnO_2 prepared at a 1 : 1 precursors ratio at 100 °C held for 2 h, were studied at the scan rates of 5, 10, 20, and 30 mV s^{-1}, as shown in Fig. 4(a), which displays the specific capacitances of 280, 270, 268, and 242 F g^{-1}, respectively, according to the eqn (2-1). The well-presented quasi-rectangular CV curves can also be observed. With the increase in scan rate, the shape of the CV curve deforms; this suggests a conjunct influence of both electric double-layer and pseudofaradaic capacitances.[36,39] At 30 mV s^{-1}, the capacitance retention was still 86.4%; therefore, the product had very good capacitive performance and cycling stability.

The galvanostatic charge–discharge (GCD) tests of δ-MnO_2 were further considered to examine the electrochemical performance, as shown in Fig. 4(b). It can be seen from Fig. 4(b) that the GCD curves present symmetrical triangles, which suggest good charging–discharging reversibility, and little *IR* drops (caused by interfacial potential of different contacting phases, $E = IR$, determined by current passing through the inner resistance). The specific capacitances can be obtained from Fig. 4(b) *via* eqn (2-2), which are 571 F g^{-1}, 286 F g^{-1}, and 140 F g^{-1} at the current densities of 0.2 A g^{-1}, 0.5 A g^{-1}, and 1 A g^{-1}, respectively. It has been reported that with an increase in current density, the storage of electrolytic ions and electrons in the crystal of MnO_2 drops. Most electrolyte ions and electrons can only approach the surface *via* adsorption–desorption to store energy, which have small specific capacitance.[40]

Fig. 4(c) illustrates the Nyquist plot of δ-MnO_2, commonly composed of a half circle at high frequency and a straight line at low frequency. This combination indicates that the electrode process was controlled by electron transport (kinetics of electrochemical reaction) and diffusion of reactant(s) or product(s) of electrode reactions.[41] At high-frequency range, the plot met the Z' axis at R_s, which is the resistance of solution, including inner resistance of the electrode material, resistance of diffusion of electrolytic ions, and contact resistance between the active species and current collector.[42,43] The resistance of solution shown in Fig. 4(c) is 1 Ω. The radius of the half circle at high frequency indicates a small resistance of electron transfer (R_{ct}) in the Faraday's process and easy passage of electrons through electrodes for energy storage.[44,45] It can also be observed from Fig. 4(c) that at low frequency, a straight line presents diffusion impedance, Z_w, with the angle between 45° and 90°, illustrating pseudocapacitive reaction under diffusion control; a line with an angle of 45°

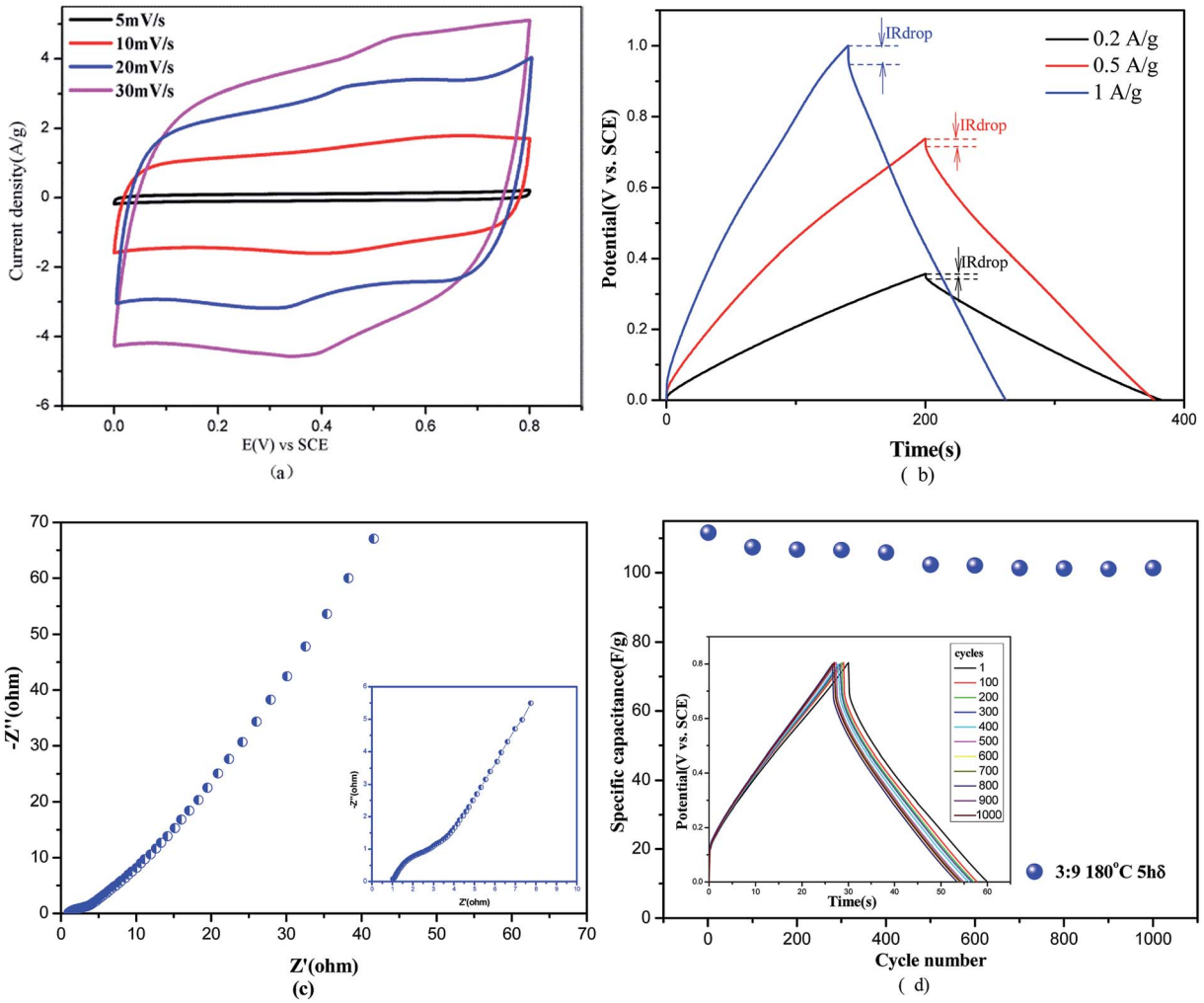

Fig. 4 (a) CV curves of δ-MnO_2 at different scan rates; (b) GCD curves of δ-MnO_2 electrodes at 0.5 A g^{-1}; (c) the Nyquist plots of the δ-MnO_2 electrodes in open potential; and (d) cycling life of the MnO_2 electrodes at 3 A g^{-1}.

indicates diffusion control and that with an angle of 90° indicates an ideal pseudocapacitive reaction.

Apart from specific capacitance, the cycling life of the material for supercapacitors is also an important aspect.[46] Fig. 4(d) displays the specific capacitance at a current density of 3 A g^{-1} for δ-MnO_2 prepared at the precursor ratio of 3 : 9, hydrothermally treated at 180 °C for 5 h. Generally, the fading of capacitance retention resulted from the irreversible product $Mn(OH)_2$, which destroyed the structure of MnO_2 and resulted in a decrease in reactive sites at the surface of electrodes, leading to an increase in inner resistance. The reduced reactive sites at the surface, causing a low utilization rate of electrode materials, lead to a drop of specific capacitance. However, in Fig. 4(d), capacitance retention of 91.8% can be observed after 1000 cycling times, and the specific capacitance only dropped by 8.6% after 1000 cycling times, presenting a relatively high cycling life.

4 Conclusions

Manganese dioxide with different crystal forms was prepared by varying the ratio of the precursor $MnSO_4 \cdot H_2O$–$KMnO_4$, reaction temperature, time, and pH values. The electrochemical performances of the prepared MnO_2 were studied as well. The conclusions are as follows:

(1) In the $MnSO_4 \cdot H_2O$–$KMnO_4$ system, MnO_2 with a controlled crystal form can be obtained *via* hydrothermal treatment from the following parameters:

α-MnO_2; $MnSO_4 \cdot H_2O$–$KMnO_4$ = 1 : 1, T = 100 °C, t = 5 h, pH at neutral;

β-MnO_2; $MnSO_4 \cdot H_2O$–$KMnO_4$ = 3 : 2, T = 180 °C, t = 5 h, pH at neutral;

δ-MnO_2; $MnSO_4 \cdot H_2O$–$KMnO_4$ = 3 : 8, T = 100 °C, t = 3 h, pH at neutral.

(2) Cationic dopants K^+ and NH_4^+ are beneficial for the formation of α-MnO_2.

(3) Specific capacitances of the prepared MnO_2 are in the following order: δ-MnO_2 > amorphous MnO_2 > α-MnO_2 > α + β-MnO_2 > β-MnO_2. Therefore, the optimal parameters for hydrothermal crystallization of powder MnO_2 as a starting material for capacitor electrode plate are $MnSO_4 \cdot H_2O$–$KMnO_4$ = 3 : 8, T = 100 °C, t = 3 h, and neutral pH.

(4) Specific capacitance of δ-MnO_2 displays a specific capacitance of 571 F g^{-1} at a current density of 0.2 A g^{-1} and a capacitance retention of 91.4% after cycling for 1000 times.

(5) The prepared MnO_2 crystal powders from the $MnSO_4 \cdot H_2O$–$KMnO_4$ system have relatively small equivalent series resistance, which is helpful for the transport of electrolytic ions and electrons. These observations display their potential capability as electrode materials for supercapacitors; however, it is necessary to significantly enhance their conductivity using heterogeneous doping during the fabrication of electrode plates from crystal powder for their practical applications in supercapacitors.

Conflicts of interest

There are no conflicts to declare.

Acknowledgements

The authors would like to thank the National Natural Science Foundation of China (NSFC Grant no. 21503146), the Yangtze Scholars and Innovative Research Team in Chinese University (IRT-17R81), and the Innovative Research Team of Tianjin Municipal Education Commission (TD12-5004) to support the work.

References

1 S. L. Zhang and N. Pan, Supercapacitors performance evaluation, *Adv. Energy Mater.*, 2015, **5**(6), 1–19.
2 H. Song, H. Zhang, C. He, *et al.*, Graphene sheets decorated with SnO_2 nanoparticles:*in situ* synthesis and highly efficient materials for cataluminescence gas sensors, *J. Mater. Chem.*, 2011, **21**(16), 5972–5977.
3 Y. Zhang, H. Feng, X. Wu, *et al.*, Progress of electrochemical capacitor electrode materials:A review, *Int. J. Hydrogen Energy*, 2009, **34**(11), 4889–4899.
4 Y. Zhang, H. Feng, X. Wu, *et al.*, Progress of electrochemical capacitor electrode materials:A review, *Int. J. Hydrogen Energy*, 2009, **34**, 4889–4899.
5 C. M. Chuang, C. W. Huang, H. Teng, *et al.*, Effects of carbon nanotube grafting on the performance of electric double layer capacitors, *Energy Fuels*, 2010, **24**, 6476–6482.
6 H. Song, H. Zhang, C. He, *et al.*, Graphene sheets decorated with SnO_2 nanoparticles:*in situ* synthesis and highly efficient materials for cataluminescence gas sensors, *J. Mater. Chem.*, 2011, **21**(16), 5972–5977.
7 Q. Feng and H. Kanoh, Manganese oxide porous crystals, *J. Mater. Chem.*, 1999, **9**(2), 319–333.
8 Y. J. Zhang, C. T. Sun, P. Lu, *et al.*, Crystallization design of MnO_2 towards better supercapacitance, *CrystEngComm*, 2012, **14**(14), 5892–5897.
9 M. Toupin, T. Brousse and D. Belanger, Charge storage mechanism of MnO_2 electrode used in aqueous electrochemical capacitor, *Chem. Mater.*, 2004, **16**(16), 3184–3190.
10 S. L. Kuo and N. L. Wu, Investigation of pseudocapacitive charge-storage reaction of $MnO_2 \cdot nH_2O$ supercapacitors in aqueous electrolytes, *J. Electrochem. Soc.*, 2006, **153**(7), A1317–A1324.
11 M. K. Song, S. Cheng, H. Chen, *et al.* Anomalous pseudocapacitivebehavior of a nanostructured, mixed-valent manganese oxide film for electrical energy storage, *Nano Lett.*, 2012, **12**(7), 3483–3490.
12 Y. Zhang, C. Sun, P. Lu, *et al.* Crystallization design of MnO_2 towards better supercapacitance, *CrystEngComm*, 2012, **14**(14), 5892–5897.
13 S. K. Meher and G. R. Rao, Enhanced activity of microwave synthesized hierarchical MnO_2 for high performance supercapacitor applications, *J. Power Sources*, 2012, **215**(4), 317–332.
14 M. Y. Yang, P. Ni, Y. Li, *et al.* Synthesis and electrochemical performance of β-MnO_2 with semi-tubular morphology, *Mater. Chem. Phys.*, 2010, **124**(1), 155–158.
15 Y. J. Zhang, C. Sun, P. Lu, *et al.*, Crystallization design of MnO_2 towards better supercapacitance, *CrystEngComm*, 2012, **14**(14), 5892–5897.
16 S. R. Majid, Controllable synthesis of flowerlike α-MnO_2 as electrode for pseudocapacitor application, *Solid State Ionics*, 2014, **262**, 220–225.
17 M. Kim, Y. Hwang and J. Kim, Graphene/MnO_2-based composites reduced *via* different chemical agents for supercapacitors, *J. Power Sources*, 2013, **239**, 225–233.
18 H. Sun, L. Mei, J. Liang, *et al.* Three-dimensional holey-graphene/niobia composite architectures for ultrahigh-rate energy storage, *Science*, 2017, **356**(6338), 599–604.
19 N. Kurra, Q. Jiang and H. N. Alshareef, A general strategy for the fabrication of high performance microsupercapacitors, *Nano Energy*, 2015, **16**, 1–9.
20 J. B. Sim, S. Mayavan and S. M. Choi, Scalable thermal synthesis of a highly crumpled, highly exfoliated and N-doped graphene/Mn-oxide nanoparticle hybrid for high-performance supercapacitors, *RSC Adv.*, 2015, **5**(53), 42516–42525.
21 Q. Y. Shan, B. Guan, S. J. Zhu, *et al.* Facile synthesis of carbon-doped graphitic C_3N_4@MnO_2 with enhanced electrochemical performance, *RSC Adv.*, 2016, **6**(86), 83209–83216.
22 S. A. Sherrill, J. Duay, Z. Gui, *et al.* MnO_2/TiN heterogeneous nanostructure design for electrochemical energy storage, *Phys. Chem. Chem. Phys.*, 2011, **13**(33), 15221–15226.
23 R. Poonguzhali, N. Shanmugam, R. Gobi, *et al.* Influence of Zn doping on the electrochemical capacitor behavior of MnO_2 nanocrystals, *RSC Adv.*, 2015, **5**(56), 45407–45415.
24 C. Pan, Y. Lv, H. Gong, *et al.* Synthesis of Ag/PANI@MnO_2 core–shell nanowires and their capacitance behavior, *RSC Adv.*, 2016, **6**(21), 17415–17422.
25 N. Subramanian, B. Viswanathan and T. K. Varadarajan, A facile, morphology-controlled synthesis of potassium-containing manganese oxide nanostructures for electrochemical supercapacitor application, *RSC Adv.*, 2014, **4**(64), 33911–33922.
26 N. Kumar, A. Sen, K. Rajendran, *et al.* Morphology and phase tuning of α-and β-MnO_2 nanocacti evolved at varying modes of acid count for their well-coordinated energy storage and

visible-light-driven photocatalytic behaviour, *RSC Adv.*, 2017, **7**(40), 25041–25053.

27 D. Deng, B. S. Kim, M. Gopiraman, *et al.* Needle-like MnO_2/activated carbon nanocomposites derived from human hair as versatile electrode materials for supercapacitors, *RSC Adv.*, 2015, **5**(99), 81492–81498.

28 S. Devaraj and N. Munichandraiah, Effect of crystallographic structure of MnO_2 on its electrochemical capacitance properties, *J. Phys. Chem. C*, 2008, **112**(11), 4406–4417.

29 M. Zhou, X. Zhang, J. Wei, *et al.* Morphology-controlled synthesis and novel microwave absorption properties of hollow urchinlike α-MnO_2 nanostructures, *J. Phys. Chem. C*, 2010, **115**(5), 1398–1402.

30 D. Kong, J. Luo, Y. Wang, *et al.* Three-Dimensional Co_3O_4@MnO_2 Hierarchical Nanoneedle Arrays: Morphology Control and Electrochemical Energy Storage, *Adv. Funct. Mater.*, 2014, **24**(24), 3815–3826.

31 S. Devaraj and N. Munichandraiah, Effect of crystallographic structure of MnO_2 on its electrochemical capacitance properties, *J. Phys. Chem. C*, 2008, **112**(11), 4406–4417.

32 H. Wang, Z. Lu, D. Qian, *et al.* Single-crystal α-MnO_2 nanorods: synthesis and electrochemical properties, *Nanotechnology*, 2007, **18**(11), 115616.

33 M. Xu, L. Kong, W. Zhou, *et al.* Hydrothermal synthesis and pseudocapacitance properties of α-MnO_2 hollow spheres and hollow urchins, *J. Phys. Chem. C*, 2007, **111**(51), 19141–19147.

34 S. H. Yu, B. Liu, M. S. Mo, *et al.*, General synthesis of single-crystal tungstate nanorodes/nanowires: a facile, low-temperature solution approach, *Adv. Funct. Mater.*, 2003, **13**(8), 639–647.

35 Y. Chen, M. L. Zhang and Z. H. Shi, Electrochemical and capacitance properties of rod-shaped MnO_2 for supercapacitor, *J. Electrochem. Soc.*, 2005, **152**(6), A1272–A1278.

36 H. Chen, S. Zhou, M. Chen, *et al.*, Reduced graphene oxide-MnO_2 hollow sphere hybrid nanostructures as high-performance electrochemical capacitors, *J. Mater. Chem.*, 2012, **22**(48), 25207–25216.

37 N. Sui, Y. Duan, X. Jiao, *et al.* Large-scale preparation and catalytic properties of one-dimensional α/β-MnO_2 nanostructures, *J. Phys. Chem. C*, 2009, **113**(20), 8560–8565.

38 G. Zhu, H. Li, L. Deng, *et al.* Low-temperature synthesis of δ-MnO_2 with large surface area and its capacitance, *Mater. Lett.*, 2010, **64**(16), 1763–1765.

39 B. Xu, S. Yue and Z. Sui, What is the choice for supercapacitors: graphene or graphene oxide?, *Energy Environ. Sci.*, 2011, **4**(8), 2826–2830.

40 X. Zeng, X. Zhao, H. Wei, *et al.* Specific Capacitance and Supercapacitive Properties of Polyaniline-Reduced Graphene Oxide Composite, *Acta Phys.-Chim. Sin.*, 2017, **33**(10), 2035–2041.

41 X. Zhao, Y. Wang, Y. Zhu, *et al.* Frequency-dependence of electric double layer capacitance of TiO_2-based composite nanotube arrays, *J. Electroanal. Chem.*, 2016, **779**, 199–206.

42 Y. Chen, M. L. Zhang, *et al.,* Electrochemical and capacitance properties of rod-shaped MnO_2 for supercapacitor, *J. Electrochem. Soc.*, 2005, **152**(6), A1272–A1278.

43 J. Gamby, P. L. Taberna, P. Simon, *et al.*, Studies and characterisations of various activated carbons used for carbon/carbon supercapacitors, *J. Power Sources*, 2001, **101**(1), 109–116.

44 D. L. Fang, Z. D. Chen, X. Liu, *et al.*, Homogeneous growth of nano-sized-$Ni(OH)_2$ on reduced graphene oxide for high-performance supercapacitors, *Electrochim. Acta*, 2012, **81**, 321–329.

45 L. Li, K. H. Seng, H. K. Liu, *et al.*, Synthesis of Mn_3O_4-anchored graphene sheet nanocomposites *via* a facile, fast microwave hydrothermal method and their supercapacitive behavior, *Electrochim. Acta*, 2013, **87**(1), 801–808.

46 Y. J. Zhang, C. T. Sun, P. Lu, *et al.*, Crystallization design of MnO_2 towards better supercapacitance, *CrystEngComm*, 2012, **14**(14), 5892–5897.